2020 IEEE/RSJ International Conference on Intelligent Robots and Systems (IROS)
October 25-29, 2020, Las Vegas, NV, USA (Virtual)

Multi-Modal Pneumatic Actuator for Twisting, Extension, and Bending

Roman Balak[1] and Yi Chen Mazumdar[1,*]

***Abstract*— Soft pneumatic actuators are commonly used in robotics for creating single-axis compression, extension, or bending motions. If these actuators are composed of compliant materials, they can also have low off-axis stiffnesses, making it difficult to restrict off-axis motions. In this work, we exploit the low off-axis stiffnesses of pneumatic actuators to design a modular actuator system that is capable of multi-modal extension, compression, two-axis bending, and twisting motions. By combining physical constraint mechanisms and motion planning, we demonstrate closed loop control with up to 24 mm of compression, 70 mm of extension, 115 degrees of bending, and 240 degrees of twisting. This actuator system is then used to illustrate several unique applications including twisting for unscrewing bottle caps and peristaltic crawling for locomotion.**

I. INTRODUCTION

Soft robotic actuators have enabled many new capabilities for traditional automation, increasing flexibility, environmental adaptability, and safe human-robot interactions through the use of built-in mechanical compliance and hyper-redundancy [1]. Robotic actuators constructed from soft materials can achieve a host of different single-axis motions including contraction, extension, rotation, or bending [2], [3], [4] that are not possible with rigid links [5]. Soft pneumatic actuators can complete bio-inspired motions [6], allow for topological programming of complex motions [7], and can have high specific forces [8]. These systems, however, also suffer from low off-axis stiffnesses, making it more difficult to restrict off-axis motion [9].

To improve off-axis stiffness and to provide actuation modes in multiple axes, several topologies have been explored including antagonistic actuators [10] and circular parallel actuator arrays [11], [12]. Antagonistic properties can be achieved through fiber-reinforcement of elastomeric enclosures [13], granular jamming [14], or topology-dependent variable stiffness mechanisms [15]. By combining antagonistic topologies with the multi-axis bending capabilities of parallel actuators, off-axis stiffnesses can be enhanced and control in multiple directions can be achieved [16], [17], [18]. Recently, parallel vacuum-driven actuators with higher stiffnesses have been developed [19], [20]. Compared to pressure-driven pneumatic actuators, however, these vacuum-driven actuators have a lower range of motion, mostly due to foam core compression ratio limitations [21], [22].

In this work, we aim exploit the low off-axis stiffness of pneumatic actuators to design a circular parallel system that is capable of multi-modal motions. The Omnidirectional Soft Robotic Actuator (OSRA) can extend, contract, bend and twist in unique ways. In this topology, extension is achieved by applying positive pressure and compression is achieved using vacuum. Bending can be achieved by applying positive pressure to the actuators on the outside of the bend or applying vacuum to the actuators on the inside of the bend. Antagonistic actuation can be achieved by combining vacuum and positive pressure on opposing sides of the multi-modal actuator. Not only does this increase the bending range but also the system stiffness compared to using solely vacuum or positive pressure. While the operation of many conventional soft pneumatic actuators is heavily dependent on the orientation of the actuator with respect to gravity due to low actuator stiffnesses [10], the OSRA has the ability to modulate its stiffness depending on the actuation strategy. This allows the OSRA to support the mass of an end effector plus additional objects and function right-side-up as well as upside-down. Furthermore, the OSRA can enter a low stiffness state to manipulate fragile objects and switch to a higher stiffness state to manipulate heavier objects.

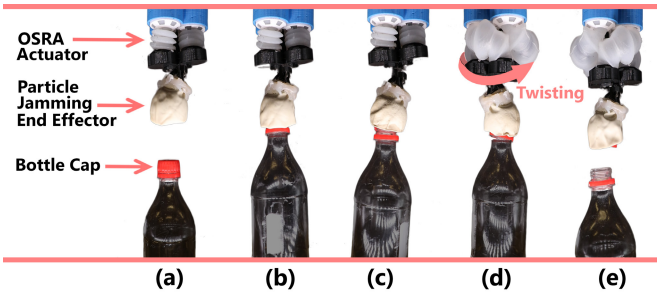

Fig. 1. a) The multi-modal actuator is used in conjunction with a particle jamming end effector to twist open a bottle cap. b) The bottle cap is put in contact with the end effector and c) the end effector hardens around the object. d) The actuator then twists until e) the cap is unscrewed.

Unlike previous work with parallel pneumatic actuators, the tunable stiffness of the OSRA described in this paper also enables unique twisting motions, as shown in Fig. 1. This can be achieved by limiting the extension or compression motion of the actuator but changing pressure in all the actuator modules simultaneously. Since the modules each have low stiffness, this combination of constraints enables rotation about the actuator's vertical z-axis. When combined with a particle jamming end effector [23], this allows the actuator to grab, unscrew, and release bottle caps. In this paper, we outline the design and manufacturing methodology for the OSRA actuator modules. Next we characterize the actuator stiffnesses, model the motion profile, and determine the actuator performance in rotation, bending, and twisting.

* Corresponding Author
[1] R. Balak and Y. C. Mazumdar are with the School of Mechanical Engineering, Georgia Institute of Technology, Atlanta, GA 30332, USA, ellen.mazumdar@me.gatech.edu

Closed loop feedback control is implemented using a three-axis gyroscope to demonstrate how the actuator could be used for various unique manipulation tasks.

II. DESIGN & MANUFACTURING

The Omnidirectional Soft Robotic Actuator is driven by a main micro-controller, a series of H-bridges, and a 9-axis (STMicro LSM9DS1) inertial measurement unit (IMU). The main actuator system is comprised of three modular axisymmetric bellows-like [24] pneumatic actuator modules arranged into a triangular footprint between two end plates (constructed with flexible TPU95 material), as illustrated in Fig. 2. Each bellows-like actuator module is connected to a single pneumatic pump (ROB-10398, 12 V) through two miniature three-way solenoid valves (AIYIMA, 6 V) that allow each module to inflate via pressure, deflate via vacuum, or vent to atmosphere. The three different chambers of each module enable the actuator to extend and compress.

Two additional pneumatic control channels are included for the particle jamming end effector and the extension constraint mechanism. The variable-stiffness particle jamming end effector uses granular materials (coffee grounds) encased in an elastic membrane with a cotton filter. When pressed against complex objects, the end effector naturally conforms around each curve. When activated by a vacuum, the particles jam against one another and solidify around complex objects thereby gripping them firmly [23]. The pneumatic control channel used for the extension constraint mechanism for twisting motions is placed directly underneath the OSRA modules. As shown in Fig. 2, the extension constraint system is composed of a flexible tube or wire sleeve that runs through an inflatable pneumatic clamping mechanism. Normally, the tube or wire sleeve can bend and twist freely. When its length is constrained via the pneumatic clamping mechanism, the distance between the end plates is locked in place. With the constraint activated, bulk changes in pressure across all the pneumatic modules results in rotations or twisting motions about the vertical z-axis.

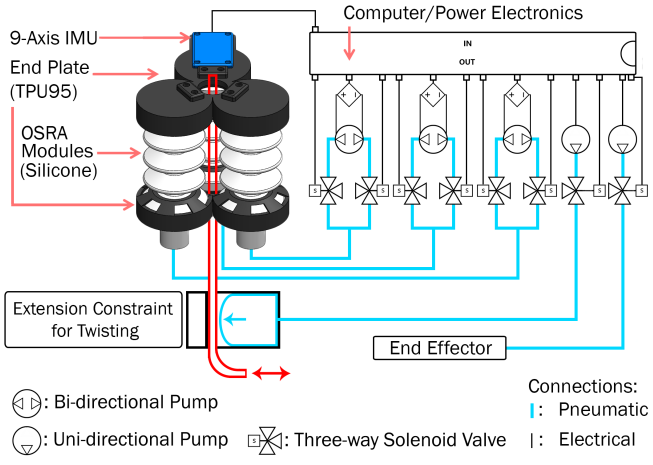

Fig. 2. The OSRA architecture is illustrated. Each of the three modules is driven by a pump attached to two three-way solenoid valves. The extension constraint and end effector are also driven with pneumatic connections.

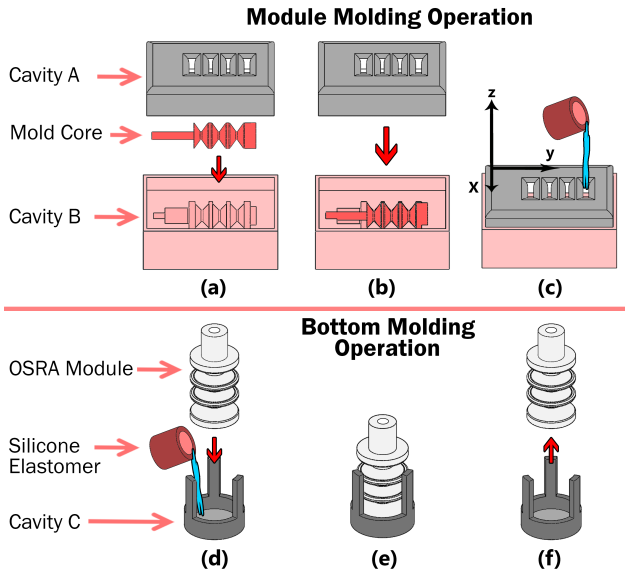

Fig. 3. The molding process for creating a single module is illustrated. (a) The three piece mold is assembled, (b) the mold core is inserted, and (c) silicone is poured into the assembled mold. The OSRA module is then removed from cavities. (d) The module is then inserted into a separate pre-filled mold (Cavity C) to seal the bottom. (e) The module is cured and (f) finally removed. Each mold is depicted here with a different color/shade.

Overall, the ideal OSRA module design has a high contraction stiffness to provide rigidity, and a lower expansion stiffness to decrease actuation time and maximize actuation range. In order to optimize the actuator stiffness for contraction, extension, bending and twisting, several different pneumatic designs were considered [24], [2]. The bellows-like design [24], was chosen due to its axisymmetry, its ability to fold onto itself in compression, and its modularity. The two-step molding process for each actuator module is described in Fig. 3. In this process, a top (Cavity A), bottom (Cavity B), and center mold piece were created in a horizontal configuration. When the three pieces are assembled, a two-part Ecoflex 00-30 silicone mixture is poured through each of the slots. Having multiple slots allows the silicone to distribute evenly and air bubbles to escape. After curing, the mold core is removed through the bottom of the actuator. The OSRA module is then placed into another pre-filled silicone mold to seal the bottom. By carefully choosing the geometry for each chamber inside each OSRA module, it is possible to scale the number of chambers to alter stiffness and range of motion without drastically changing control techniques.

Several different geometries and materials were tested. Stiffer silicones and thicker walls allowed the actuator to hold a more stable rest shape and increased motion repeatability. However, this also limited the overall range of motion. At higher levels of inflation, the actuators also begin to expand or balloon horizontally. While expansion of the neck portions of the chambers is desirable for creating vertical extension, ballooning at the crest portions causes undesirable collisions and increases friction between modules. Since air pressure acts uniformly on the inner walls, minimizing vertical surface area of the inner walls near the crest regions decreases the ballooning effect. Conversely, maximizing the vertical

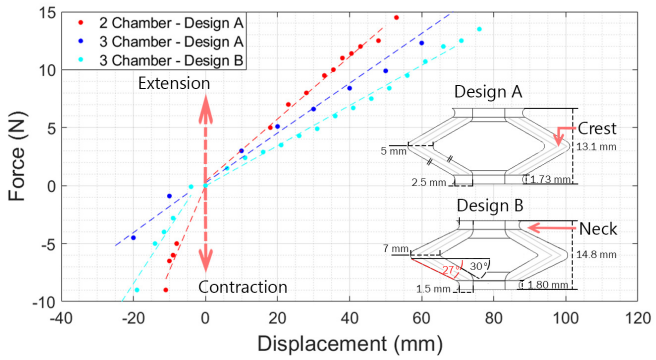

Fig. 4. Passive extension and compression forces required to move each model for three different module designs are shown. Two different chamber designs with the same outer diameter at the crest (30 mm) are compared.

surface area of the inner walls of the neck region increases the desirable extension effect. Thus, minimizing the internal vertical surface area near the crest and maximizing the internal vertical surface area near the neck increases the overall length of the modules at maximum input pressure with reduced detrimental actuator ballooning.

The extension and compression force characteristics for two different chamber designs are compared in Fig. 4. For these experiments, a force gauge placed in-line with the actuator is used to measure the passive elastic force of one module as it was passively extended or compressed. In chamber design A, 30° parallel internal and external walls were used with a neck width of 2.5 mm and a crest width of 5 mm. In chamber design B, the outer diameter remains unchanged at 30 mm while the external wall angle is reduced to 27° with an internal wall angle of 30°. A smaller external bellows angle allowed the actuator to taper at the neck thereby promoting extension. The neck width is reduced to 1.5 mm and the crest width is increased to 7 mm. The chamber has a 13 mm outer diameter at the neck and a chamber-to-chamber distance of 13 mm.

In extension, the stiffness depends on the module design and scales almost proportionally with the number of chambers. In contraction the maximum compression is constrained by the end plate, which leads to the non-linear stiffness effects that are not proportional to the number of chambers. The total range of motion (defined as the difference between the length of the module in minimum vacuum pressure and maximum pump pressure) for the 2 chamber, 3 chamber design A, and 3 chamber design B systems were 45 mm, 90 mm, and 94 mm, respectively. The expansion stiffnesses were 269 N/m, 225 N/m and 174 N/m while the contraction stiffnesses were 733 N/m, 215 N/m, and 477 N/m, respectively. Overall, the 2 chamber design had higher stiffnesses but a lower range of motion, making it less desirable. The 3 chamber design B system showed the highest ratio of contraction to expansion stiffness, making it the best candidate. The final design used the 3 chamber design B configuration and each module was 26.2 g. Excluding the electronics, the total OSRA actuator was ∼150 g.

III. MODELING & CHARACTERIZATION

Unlike traditional robotic actuators with rigid links and well-defined joint motions, the OSRA system has several possible extension, compression, bending, and twisting actuation modes. By carefully characterizing and modeling the open loop performance of each of these modes, it is then possible to plan useful motions using this soft actuator. In this work, a bulk modeling approach informed by experimental data, rather than a finite element modeling approach [25], is taken. Figure 5 shows the coordinate system for the orientation angle θ, bend angle ϕ, and twisting angle ζ.

The placement of the three actuator modules and the geometric constraints produces two different types of bending behaviors along the primary and secondary axes for each actuator module. Here, motions along the primary axes occur when there are two modules opposite to the actuation direction, defined with orientation angles that are $\theta_{Desired} = 120°n$ for $n \in \mathbb{Z}$. To achieve bending along primary axes, it is possible to activate a single actuator module in vacuum and two modules with positive pressure in an antagonistic fashion. Motions along the secondary axes occur when there is one module opposite to the actuation direction, defined with orientation angles that are $\theta_{Desired} = 120°n + 60°$. Secondary axes can be accessed antagonistically with two modules in vacuum and one module with positive pressure. Based on these definitions and the geometric constraints of the triangular top end plate, it is clear that the primary axes are capable of achieving larger ϕ bend angles (up to $\phi_{max} = 115°$) than the secondary axes (up to $\phi_{max} = 95°$).

To model the actuator stiffnesses in different modes, a force balance is employed on each module such that,

$$F_{External} + F_{Output} = F_{Pressure} - F_{Elastic} - F_{Damping} - F_{Inertia}, \quad (1)$$

which accounts for input pressure forces, external forces, output forces, and dynamic forces. By linearizing about the equilibrium position, we can assume linear models for elastic deformation of the silicone $F_{Elastic} = k_0 L(t)$ and input force due to pressure $F_{Pressure} = C_0 t$, where k_0 is the bulk spring constant in extension or compression, $L(t)$ is the length of the each module, t is the activation time of the pump and valves, and C_0 is the scaling constant describing the pressure buildup in the actuator over time. At steady state with no

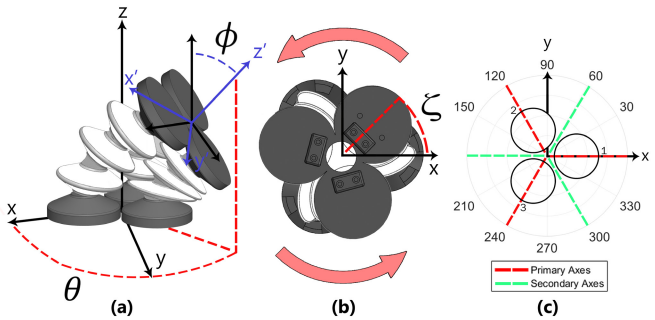

Fig. 5. (a) A side view shows actuator orientation angle θ and end plate bend angle ϕ. (b) A top view shows the angular twisting angle ζ of the top end plate relative to the bottom end plate. (c) A top view shows the module positions relative to the primary and secondary bending axes.

external forces, the input force from pressure balances with the elastic force. Therefore, a linear relationship can be obtained between the length and the activation time of each actuator module $L(t) = (C_0 t)/k_0$ for small displacements. In reality, the length does not increase linearly and higher order polynomials can be used to model $L(t)$.

In order to determine actuator orientation and bend angle from module lengths, a geometric model is applied. In this model, the orientation angle θ is first found by using the steady state actuator module lengths $L_1(t_1)$, $L_2(t_2)$, and $L_3(t_3)$ using the known activation times. These module lengths are then used to estimate the height of the vertices of the top end plate. By taking the cross product of the lines between vertices $\vec{d}_{ij}$ of the triangular end plate, it is possible to determine the angle of the vector $\vec{N}$ normal to the end plate surface, $\vec{N} = (\vec{d}_{12} \times \vec{d}_{23}) + (\vec{d}_{31} \times \vec{d}_{12}) + (\vec{d}_{23} \times \vec{d}_{31})$. This is then used to estimate the orientation angle $\theta = \tan^{-1}(N_y/N_x)$. To incorporate physical constraints for intermediate ϕ bending angles, linear interpolation is used between primary and secondary bending axes such that $M(\theta) = |1 - \mathrm{mod}(\theta, 120°)/60°|$. This can then be used to correct estimates of ϕ for intermediate angles using $K_\theta = R + (1-R)M(\theta)$, where $R = \phi_{max,2}/\phi_{max,1}$ is the ratio between the maximum bend angle of secondary versus primary axes.

Once the orientation angle θ are known, it is possible to estimate the total bend angle ϕ by using a circular arc approximation. When the modules are operating antagonistically, the modules under positive pressure revolve in a circular path around the modules in vacuum. If the actuators are operated in a non-antagonistic manner, the actuator bend path is more complex and cannot be approximated with a circular arc. Therefore, only antagonistic bending motions are considered for modeling with bend angles of,

$$\phi = K_\theta \frac{\phi_{max}}{L_{max}} L(t), \tag{2}$$

up to the maximum bend angle ϕ_{max} and actuator length L_{max} associated with each θ. This simple geometric model

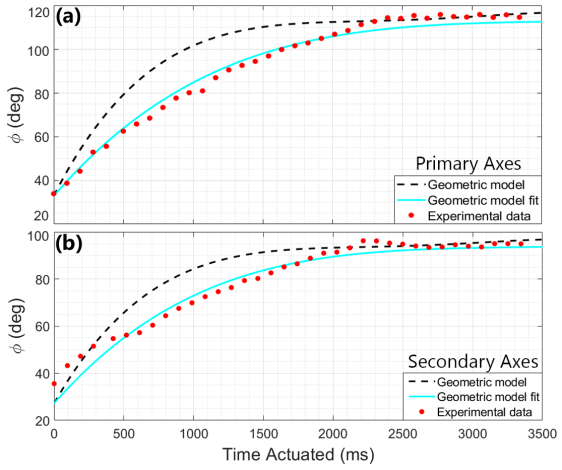

Fig. 6. The experimentally measured bend angle, ϕ, for low speed motions as a function of actuation time along (a) the primary axes and (b) the secondary axes are compared with the first-principles geometric model and a modified geometric model fit.

for bend angle, ϕ, as a function of actuation time is compared with experimental data collected using integrated IMU gyroscope angular rates, as shown in Fig. 6 for actuation along the primary and secondary axes. While the geometric model and experimental data are similar, it is clear that additional effects make the real system operate slower than predicted by the model. This effect can be driven by non-linearities in the actuator input pressure model and unmodeled force/torque transfer between different modules. Since the simple geometric model does not incorporate these effects, the geometric model for $L(t)$ can be modified using a scaling factor K_{ss}, such that the experimental data in Fig. 6 can be fit to the geometric model through the relationship $L_f(t) = K_{ss} L(t)$. This model can then be used to predict the orientation and bend angle from any set of module actuation times or to plan the inputs needed to achieve other multi-modal motions.

Next, the compound total elastic force for the entire OSRA actuator can be characterized for different bend angles, taking into account force/torque transfer between different modules. This compound total elastic force can be estimated by integrating the compound angular stiffness for extension as a function of actuator activation time,

$$F_{elastic} \approx k_0 L(t,\theta) \approx \int_0^{\phi(t,\theta)} k_\phi(t,\theta)\, \mathrm{d}\phi, \tag{3}$$

where $k_\phi(t,\theta)$ is the measured compound angular stiffness of the actuator. One example is illustrated in Fig. 7 for the secondary axis angle of $\theta = 60°$. With antagonistic actuation, the contraction and expansion angular stiffnesses exhibit inverted behaviours as the bend angle increases. The use of antagonistic actuation (at least one module in vacuum) significantly increases both the expansion and contraction angular stiffnesses. The ability to switch modules on the inside of the bend between atmospheric pressure and vacuum allows the OSRA to tune its stiffness and load bearing capacity on demand. Next, a high-order polynomial is fit to the antagonistic actuation data and integrated according to Eq.(3) to determine the compound elastic force as a function of ϕ. The maximum elastic force is then 17 N at $\phi_{max} = 115°$ along the primary axes and 12 N at $\phi_{max} = 94°$ along the secondary axes, as shown in Fig. 8.

The compound linear stiffness can also be roughly esti-

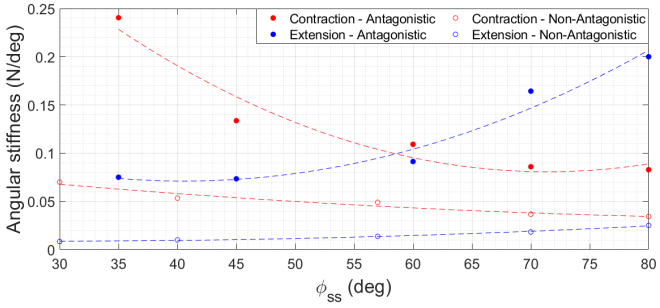

Fig. 7. Angular stiffnesses along the secondary axes ($\theta = 60°$) as a function of the steady state ϕ_{ss} angle in open loop are illustrated. In the antagonistic state, one module is in positive pressure and two modules are in vacuum. In the non-antagonistic state, one module is in positive pressure and two modules are at atmospheric pressure. Polynomials are fit to each state.

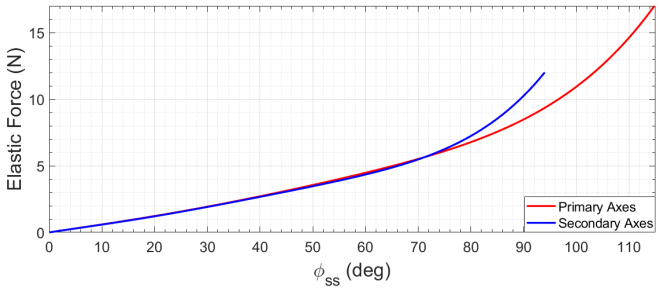

Fig. 8. A model for the total elastic force counteracting the internal pressure of the modules is illustrated as a function of the steady state ϕ_{ss} angle.

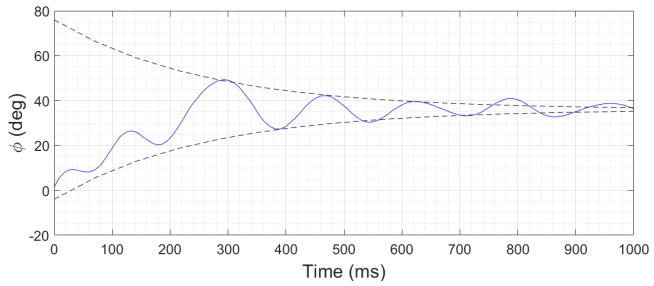

Fig. 9. The open loop step response of the bend angle ϕ in antagonistic mode is shown for the OSRA actuator.

mated by dividing the compound elastic force by the length of the modules. For motion along the primary axes the force is linear with respect to time up to 45 mm of extension. For the secondary axes, the force is linear up to 35 mm of extension. Within the linear region, $k_0 = 49.7$ N/m along the primary axes and $k_0 = 20.6$ N/m along the secondary axes. These measurements produce a compound linear stiffness of, $k_0(\theta) = 20.6 + 29M(\theta)$ N/m, as a function of orientation angle θ valid up to $k_{max}(\theta) = 183.88 + 79.07M(\theta)$ N/m. The average stiffnesses between 35 mm and 60 mm for primary axes and secondary axes are much higher at 260 and 180 N/m, respectively. The constants for the input pressure could also be determined using steady state measurements and were found to be $C_0 = 0.008$ along the primary axes and $C_0 = 0.007$ along the secondary axes.

The open loop bend angle step response of the actuator can be seen in Fig. 9 with a natural frequency of $\omega_n = 6.67$ Hz. By examining the envelope of the oscillations, the damping ratio was determined to be 0.1. Thus, $F_{Damping} = 0.59\dot{L}$ from these measurements, allowing the right hand side of Eq.(1) to be fully characterized as a function of θ and ϕ.

IV. CLOSED LOOP PERFORMANCE

Performance metrics for the OSRA were characterized and are listed in Table I. The specific force, which characterizes the force to weight ratio, for this actuator is 108 N/kg. From full contraction to full extension, the total range of motion is 94 mm with a maximum extension force of 14.4 N and a maximum compression force of 13.1 N. In the twisting mode, which can rotate $\pm$ 120°, the maximum output torque was found to be 0.36 N·m.

Three separate closed loop control schemes were implemented to improve positioning accuracy and minimize actuator settling time. These control schemes consist of orientation control (θ), bend angle control (ϕ), and twisting control (ζ). The θ, ϕ, and ζ angular measurements were collected from integrated gyroscope signals from the IMU, similar to [26], [27]. The control inputs were different duty cycles and actuation times applied to the valves and pumps.

When the end plate locations are locked via the extension constraint mechanism, inflating all chambers results in a twisting motion around the z-axis. For twisting ζ control, only a simple proportional controller was needed due to the end plate constraint and high physical damping. An example of how the twisting motion can be used for complex manipulation is demonstrated in Fig. 1, where the OSRA is used to unscrew a bottle cap. The direction of rotation can be controlled using a short (500 ms) motion planning operation. The motion sequence initiates with one module being inflated, then suction is applied to the module that is in the desired direction of rotation. This causes a small tilt. Then, the extension constraint mechanism is used to lock the end plate distance. Finally, all actuators are inflated to induce rotation into the planned direction. Examples of planned clockwise and counterclockwise twisting motions can be found in the video accompanying this paper.

In Fig. 10, closed loop twisting motions from $\zeta = 0°$ to 120° are demonstrated. In this figure, the slew rate of the first step up to 40° was observed to be 160°/s. This then decreases to 73°/s when the angle increased to 80°. Finally, the slew rate decreases to 25°/s at an angle of 120°. This decrease in slew rate is due the modules reaching their maximum length and pressure limits, which results in nonlinear actuation effects associated with ballooning. This phenomena can be observed in Fig. 10, where at 120° the actuator is significantly larger than for other cases.

The same effect can be observed with control along the primary bending axes ϕ, as shown in Fig. 11. Up to a bend angle of $\phi = 30°$ the slew rate was 150°/s, which decreases to 60°/s and 34°/s as the bend angle was increased to $\phi = 60°$ and $\phi = 90°$, respectively. The relationship for the end plate angle outlined in Eq.(2) is used in conjunction with the gyroscope measurement and a proportional controller to enable fine tuning of the bend angle position.

Orientation control of the θ angle is the most complex, requiring a combination of proportional, derivative and integral terms across multiple actuators in order to minimize the settling time. Fig. 12 illustrates the closed loop control for the actuator when moving from 0° to 120° to 240°.

TABLE I
OSRA ACTUATOR PERFORMANCE

Property	Value	Units
Specific Force	108	N/kg
Extension & Contraction Range	-24 to 70	mm
Primary Bending Range	115	degrees
Secondary Bending Range	94	degrees
Peak Extension Force	14.4	N
Peak Contraction Force	13.1	N
Twisting Range	-120 to 120	degrees
Peak Twisting Torque	0.36	N·m

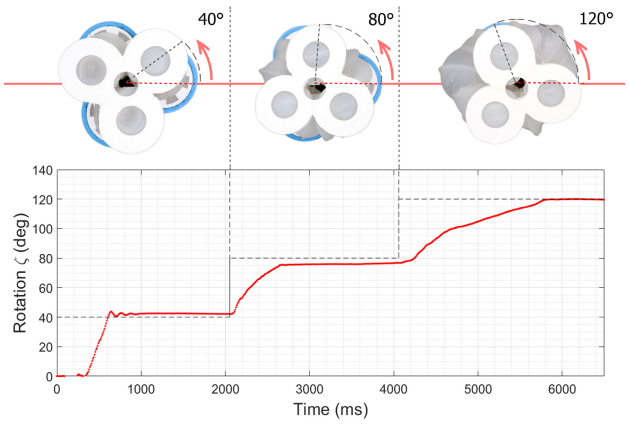

Fig. 10. Time response for z-axis twisting for $\zeta_{Des} = 0°, 40°, 80°$, and $120°$ are shown here and in the accompanying video.

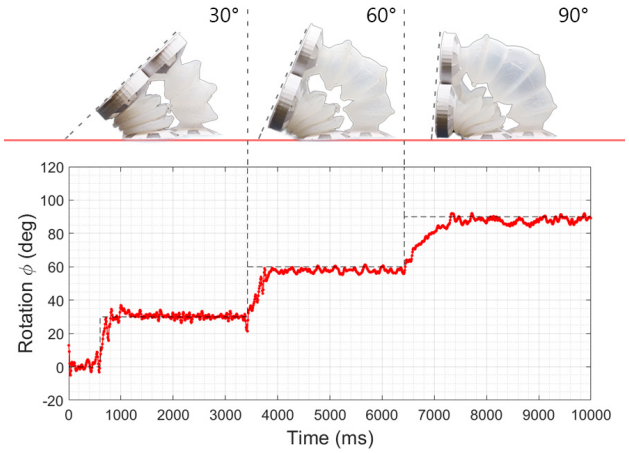

Fig. 11. Time response of ϕ bending control along the primary axes for $\phi_{Des} = 0°, 30°, 60°$, and $90°$ are shown here and in the accompanying video.

For angles between $60° < \theta_{Desired} \leq 180°$ modules 1 and 3 are controlled and module 2 is placed under vacuum. For angles between $180° < \theta_{Desired} \leq 300°$, modules 1 and 2 are controlled and module 3 is placed under vacuum. Finally, for angles between $300° < \theta_{Desired} \leq 60°$, modules 2 and 3 are controlled and module 1 is put under vacuum. As illustrated in Fig. 13, the settling time is lowest along the primary axes since two modules are inflated and under closed loop control. The location of the settling time minima is less consistent along secondary axes because one of the two modules being controlled is likely in full contraction, increasing its extension velocity and settling time. Overall, the response time for orientation control is not limited by the actuator slew rate but is instead limited by the response time of the solenoid valves (50 ms) and the settling time for oscillations (2 s). Orientation θ and bend angle ϕ control can also be implemented together. When $\phi_{Error} > 0$ the modules use inflation to tune orientation θ. When $\phi_{Error} < 0$ the modules use vacuum to tune orientation θ.

Fig. 14 demonstrates a second complex multi-modal application for the OSRA actuator. Here, a motion planning algorithm was implemented to show peristaltic locomotion at a speed of ∼3 mm/s. The motion sequence closely emulates the peristaltic locomotion of a worm, consisting of three

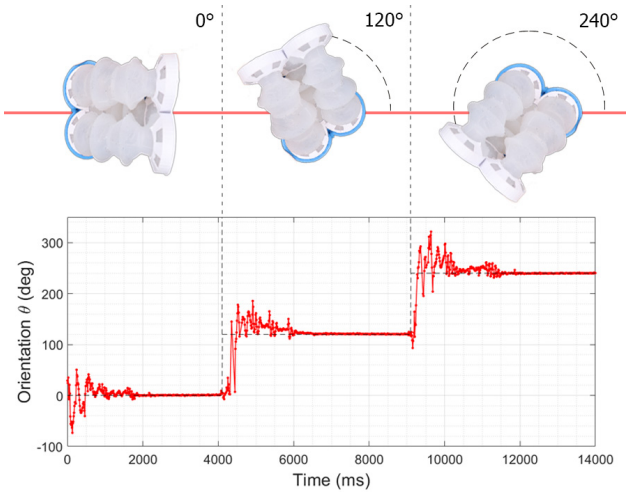

Fig. 12. Time response for θ control for $\theta_{Des} = 0°, 120°$, and $240°$ are shown here and in the accompanying video.

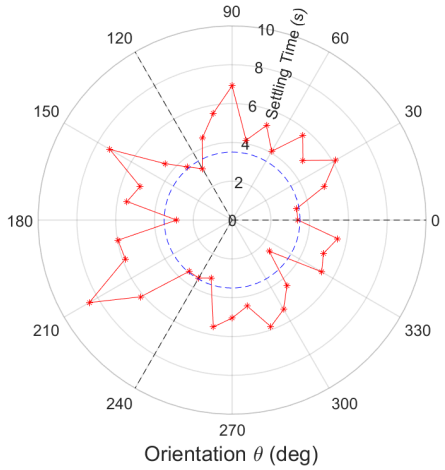

Fig. 13. Average settling times (defined as $\pm 2°$) for $\phi_{Des} = 60°$ at various orientation angles θ. All time responses on the primary axes have a settling time below 3.5 s as illustrated by the blue dotted circle.

separate strokes [28] cycled once every 3.5 seconds. First, the bottom two actuators are inflated while the top one remains in vacuum. Next, the top actuator is inflated while a vacuum is applied to the bottom two. Finally, the actuator is contracted, allowing the OSRA to move ∼10 mm per stroke.

V. CONCLUSION

In this paper, a soft actuator composed of parallel pneumatic modules and capable of a wide-range of multi-modal motions is presented. The design of individual chamber geometries and selection of actuator stiffnesses are discussed. A bulk model is then presented to assist with accurate motion planning. Not only can this actuator achieve closed-loop extension, compression, and bending in multiple directions, but it also exploits physical constraint mechanisms to achieve unique twisting motions. Additionally, variable stiffness allows users to grip fragile and heavy objects with the same actuator. Finally, this novel actuator is used to demonstrate crawling motions and to unscrew bottle caps.

Future improvements to the OSRA actuator include new

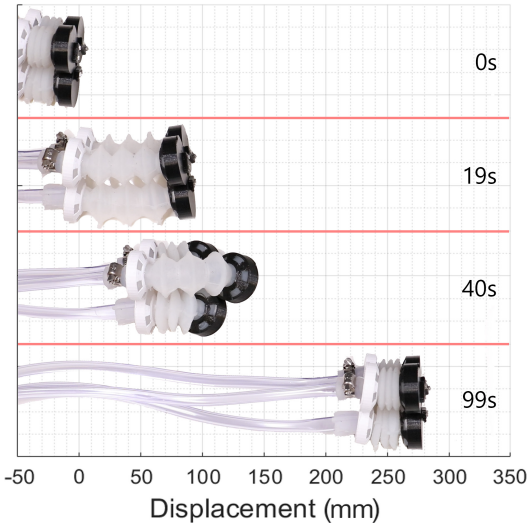

Fig. 14. Crawling motion is illustrated here and in the accompanying video by using a sequence of bending, contraction and extension motions.

end plate designs to reduce range-of-motion restrictions, improved orientation control, alternative constraint mechanisms, and the addition of soft bend sensors [29] or magnetic position sensors [30] for enhanced closed-loop control. Furthermore, streamlining and combining several OSRA actuators would allow for more complex applications such as motion planning for complex twisting motions, grasping for assembly tasks, compound manipulation, snake-like locomotion, or legged soft robot locomotion.

ACKNOWLEDGMENT

The authors would like to thank the Georgia Tech Institute for Robotics and Intelligent Machines and the President's Undergraduate Research Awards program for their support.

REFERENCES

[1] D. Trivedi, C. D. Rahn, W. M. Kier, and I. D. Walker, "Soft robotics: Biological inspiration, state of the art, and future research," *Appl. Bionics Biomech.*, vol. 5, no. 3, pp. 99–117, 2008.

[2] B. Mosadegh, P. Polygerinos, C. Keplinger, S. Wennstedt, R. F. Shepherd, U. Gupta, J. Shim, K. Bertoldi, C. J. Walsh, and G. M. Whitesides, "Pneumatic networks for soft robotics that actuate rapidly," *Adv. Funct. Mater.*, vol. 24, no. 15, pp. 2163–2170, 2014.

[3] M. Schaffner, J. A. Faber, L. Pianegonda, P. A. Rühs, F. Coulter, and A. R. Studart, "3d printing of robotic soft actuators with programmable bioinspired architectures," *Nat. Commun.*, no. 9, p. 898, 2018.

[4] T. Wang, L. Ge, and G. Gu, "Programmable design of soft pneu-net actuators with oblique chambers can generate coupled bending and twisting motions," *Sensors Actuat. A*, vol. 271, pp. 131–138, 2018.

[5] T. M. Miller-Jackson, J. Li, R. F. Natividad, and R. C. Yeow, "STAS: An antagonistic soft pneumatic actuator assembly for high torque output," in *IEEE International Conference on Soft Robotics*, 2019, pp. 43–48.

[6] S. Kim, C. Laschi, and B. Trimmer, "Soft robotics: a bioinspired evolution in robotics," *Trends Biotechnol.*, vol. 31, pp. 287–294, 2013.

[7] P. Polygerinos, N. Correll, S. A. Morin, B. Mosadegh, C. D. Onal, K. Petersen, M. Cianchetti, M. T. Tolley, and R. F. Shepherd, "Soft robotics: Review of fluid-driven intrinsically soft devices: Manufacturing, sensing, control, and applications in human-robot interaction," *Adv. Eng. Mater.*, vol. 19, no. 12, p. 1700016, 2017.

[8] G. Miron, B. Bédard, and J.-S. Plante, "Sleeved bending actuators for soft grippers: A durable solution for high force-to-weight applications," *Actuators*, vol. 7, p. 40, 07 2018.

[9] P. Boyraz, G. Runge, and A. Raatz, "An overview of novel actuators for soft robotics," *Actuators*, vol. 7, no. 3, p. 48, 2018.

[10] K. Althoefer, "Antagonistic actuation and stiffness control in soft inflatable robots," *Nat. Rev. Mater.*, vol. 3, no. 6, pp. 76–77, 2018.

[11] M. A. Robertson and J. Paik, "New soft robots really suck: Vacuum-powered systems empower diverse capabilities," *Sci. Robot.*, vol. 2, no. 9, p. eaan6357, 2017.

[12] M. A. Robertson, H. Sadeghi, J. M. Florez, and J. Paik, "Soft pneumatic actuator fascicles for high force and reliability," *Soft Robot.*, vol. 4, no. 1, pp. 23–32, 2017.

[13] R. Deimel and O. Brock, "A compliant hand based on a novel pneumatic actuator," in *IEEE International Conference on Robotics and Automation*, 2013, pp. 2047–2053.

[14] A. Jiang, A. Ataollahi, K. Althoefer, P. Dasgupta, and T. Nanayakkara, "A variable stiffness joint by granular jamming," in *ASME International Design Engineering Technical Conferences and Computers and Information in Engineering Conference*, 2012, pp. 267–275.

[15] T. Sun, Y. Chen, T. Han, C. Jiao, B. Lian, and Y. Song, "A soft gripper with variable stiffness inspired by pangolin scales, toothed pneumatic actuator and autonomous controller," *Robot. Cim.-Int. Manuf.*, vol. 61, p. 101848, 2020.

[16] J. Bishop-Moser, G. Krishnan, C. Kim, and S. Kota, "Design of soft robotic actuators using fluid-filled fiber-reinforced elastomeric enclosures in parallel combinations," in *IEEE/RSJ International Conference on Intelligent Robots and Systems*, 2012, pp. 4264–4269.

[17] M. B. Pritts and C. D. Rahn, "Design of an artificial muscle continuum robot," in *IEEE International Conference on Robotics and Automation*, vol. 5, 2004, pp. 4742–4746.

[18] D. Bruder, A. Sedal, R. Vasudevan, and C. D. Remy, "Force generation by parallel combinations of fiber-reinforced fluid-driven actuators," *IEEE Robot. Autom. Lett.*, vol. 3, no. 4, pp. 3999–4006, 2018.

[19] J. Walker, T. Zidek, C. Harbel, S. Yoon, F. S. Strickland, S. Kumar, and M. Shin, "Soft robotics: A review of recent developments of pneumatic soft actuators," *Actuators*, vol. 9, no. 1, p. 3, 2020.

[20] D. Yang, "Soft pneumatic actuators using negative pressure," Ph.D. dissertation, Harvard University, 2016.

[21] M. A. Robertson and J. Paik, "Low-inertia vacuum-powered soft pneumatic actuator coil characterization and design methodology," in *IEEE International Conference on Soft Robotics*, 2018, pp. 431–436.

[22] D. Yang, M. S. Verma, J.-H. So, B. Mosadegh, C. Keplinger, B. Lee, F. Khashai, E. Lossner, Z. Suo, and G. M. Whitesides, "Buckling pneumatic linear actuators inspired by muscle," *Adv. Mater. Technol.*, vol. 1, no. 3, p. 1600055, 2016.

[23] J. Amend, N. Cheng, S. Fakhouri, and B. Culley, "Soft robotics commercialization: Jamming grippers from research to product," *Soft Robot.*, vol. 3, no. 4, pp. 213–222, 2016.

[24] G. Dämmer, S. Gablenz, A. Hildebrandt, and Z. Major, "Polyjet-printed bellows actuators: Design, structural optimization, and experimental investigation," *Front. Robot. AI*, vol. 6, p. 34, 2019.

[25] W. Hu, R. Mutlu, W. Li, and G. Alici, "A structural optimisation method for a soft pneumatic actuator," *Robotics*, vol. 7, no. 2, p. 24, 2018.

[26] Y. Chen, J. M. Oliveira, and I. W. Hunter, "Sensor architecture for a two-actuator robotic endoscope tip," in *IEEE Engineering in Medicine and Biology Conference*, 2011, pp. 8340–8343.

[27] Y. Chen, J. Liang, and I. W. Hunter, "Modular continuum robotic endoscope design and path planning," in *IEEE International Conference on Robotics and Automation*, 2014, pp. 5393–5400.

[28] M. Calisti, G. Picardi, and C. Laschi, "Fundamentals of soft robot locomotion," *J. R. Soc. Interface*, vol. 14, no. 130, p. 20170101, 2017.

[29] Y. Chen, J. M. Oliveira, and I. W. Hunter, "Two-axis bend sensor design, kinematics and control for a continuum robotic endoscope," in *IEEE International Conference on Robotics and Automation*, 2013, pp. 704–710.

[30] Y. Chen, A. Mazumdar, C. F. Brooks, B. G. van Bloemen Waanders, S. D. Bond, and M. B. Nemer, "Remote distributed vibration sensing through opaque media using permanent magnets," *IEEE Trans. Magn.*, vol. 54, no. 6, pp. 1–13, 2018.